Т. 89, № 1 **ЖУРНАЛ ПРИКЛАДНОЙ СПЕКТРОСКОПИИ** ЯНВАРЬ — ФЕВРАЛЬ 2022
V. 89, N 1 **JOURNAL OF APPLIED SPECTROSCOPY** JANUARY — FEBRUARY 2022

SPECTRAL AND PLASMA CHARACTERISTICS OF ATMOSPHERIC PRESSURE GLOW DISCHARGE BETWEEN SOLUTION CATHODE AND HOLLOW METAL ANODE WITH MINIATURE ARGON GAS FLOW[**]

P. Zheng[*], R. Liu, J. Wang, Yu. Luo, H. Zhao, X. Mao, Ch. Lai

Chongqing Municipal Level Key Laboratory of Photoelectronic Information Sensing and Transmitting Technology, College of Optoelectronic Engineering at Chongqing University of Posts and Telecommunications; Chongqing, China; e-mail: zhengpc@cqupt.edu.cn

An atmospheric pressure glow discharge between solution cathode and hollow anode with miniature argon gas flow was built. The spectra of excited species (including NO, O, N_2, H, and Ar) in the plasma and the characteristic parameters of the plasma were investigated. The result shows that argon gas increases the spectral intensity of the high energy species in the cathode and anode. Additionally, the plasma image and the distribution of sound frequency are collected. As the flow rate of argon increases, the plasma volume is significantly smaller. The audio signal in the high frequency band (~10000 Hz) is weakened while the argon flow rate increases. The range of sound distribution within the low frequency band becomes wider (from ~2000–3000 to ~2000–5000 Hz). This shows that argon can affect the stability of the plasma and the collision of internal particles. We also measured the spectral parameters (including electron excited temperature, rotational temperature, and electron number density). The result shows that improvement of the argon flow rate in the near cathode region can also increase the plasma parameters. The electron excited temperature and electron number density are higher in the region near the anode.

Keywords: *atmospheric pressure glow discharge, hollow anode, plasma temperature, electron number density.*

СПЕКТРАЛЬНЫЕ И ПЛАЗМЕННЫЕ ХАРАКТЕРИСТИКИ ТЛЕЮЩЕГО РАЗРЯДА АТМОСФЕРНОГО ДАВЛЕНИЯ МЕЖДУ КАТОДОМ-РАСТВОРОМ И ПОЛЫМ МЕТАЛЛИЧЕСКИМ АНОДОМ С МИНИАТЮРНЫМ ПОТОКОМ ГАЗА АРГОНА

P. Zheng[*], R. Liu, J. Wang, Yu. Luo, H. Zhao, X. Mao, Ch. Lai

УДК 533.9;537.525.1

Колледж оптоэлектронной инженерии Чунцинского университета почты и телекоммуникаций, Чунцин, Китай; e-mail: zhengpc@cqupt.edu.cn

(Поступила 20 ноября 2020)

Создан тлеющий разряд атмосферного давления между катодом-раствором и полым анодом с миниатюрным потоком аргона. Исследованы спектры возбужденных частиц (NO, O, N_2, H и Ar) в плазме и характерные параметры плазмы. Показано, что аргон увеличивает спектральную интенсивность высокоэнергетических частиц в катоде и аноде. Дополнительно получены изображение плазмы и распределение звуковой частоты. По мере увеличения скорости потока аргона объем плазмы значительно уменьшается. Звуковой сигнал в высокочастотном диапазоне (~10000 Гц) ослабевает, а скорость потока аргона увеличивается. Диапазон распространения звука в области низких частот становится шире (от ~2000–3000 до ~2000–5000 Гц). Это свидетельствует о том, что аргон может влиять на стабильность плазмы и столкновение внутренних частиц. Измерены спектральные параметры – температура возбуждения электронов, температура вращения и плот-

---

[**] Full text is published in JAS V. 89, No. 1 (http://springer.com/journal/10812) and in electronic version of ZhPS V. 89, No. 1 (http://www.elibrary.ru/title_about.asp?id=7318; sales@elibrary.ru).

ность электронов. Показано, что увеличение скорости потока аргона в прикатодной области может увеличивать параметры плазмы. Температура возбуждения электронов и плотность электронов выше в прианодной области.

Ключевые слова: *тлеющий разряд атмосферного давления, полый анод, температура плазмы, плотность электронов.*

Introduction. Glow discharge generated with solution-electrodes has gradually attracted more attention due to its application in spectral detection and analysis [1–4]. Compared with other spectral analysis technologies, solution cathode glow discharge (SC-GD) and related discharges have the advantages of working in atmospheric air, low power, low gas consumption, and moderate spectral resolution requirements [5], which means that SC-GD and its related discharges are more efficient. Therefore, it can be seen that they may become portable spectroscopic analysis instruments [6]. T. Cserfalvi et al. [7] first proposed a glow discharge with solution cathode to analyze atomic spectroscopy and electrolyte-cathode discharge (ELCAD) in 1993. Since then, many scholars have adjusted the device in order to further improve the detection performance [8]. The early version consumed a lot of liquid and had poor stability. M. R. Webb et al. [9] improved the cathode to reduce the flow rate to ~0.25–3.5 mL/min and called the device a solution cathode glow discharge (SCGD). The system has broad prospects for the detection of liquid metal elements. Later, C. D. Quarles et al. [8] designed an atmospheric pressure glow discharge device with low currents (<20 mA) and low solution flow rates (<50 μL/min), which is the liquid sampling-atmospheric pressure glow discharge (LS-APGD). As a low-power ionization source, LS-APGD is a relatively simple alternative for atomic mass spectrometry applications. R. K. Marcus et al. [10] applied LS-APGD to the analysis of green tea extract and raw leaves, coffee beans, and other substances.

In the overwhelming LS-APGD systems, the structure of the cathode and anode of the discharge system is different. In recent years, the introduction~~s~~ of argon or helium jets from a hollow anode enhanced the stability of the plasma and cooled the excitation source of the glow discharge generated with solution-electrodes [11, 12]. In addition, a hollow anode can be employed as the system's sampling inlet method, such as the introduction of photochemical vaporization [13] and ultrasonic atomization [14, 15]. K. Greda et al. used optical emission spectroscopy to measure mercury in water samples and moss by coupling atmospheric pressure glow micro-discharges with cold steam [16, 17]. However, research on the effects of the inlet argon gas on the spectral and plasma characteristics is needed.

In order to understand the chemical and physical processes occurring in the excitation source and evaluate the excitation performance of glow discharge with solution-electrodes, the plasma parameters, including electron excited temperature, rotational temperature, and electron number density, are to be measured [18]. T. Verreycken et al. used emission spectrum, Raman scattering, and Rayleigh scattering to determine the gas temperature of an atmospheric air glow discharge with water electrode, and the spatial distribution of gas temperature was explored. The results show that the gas temperature measured by these methods is basically consistent [19]. The characteristic parameters of plasma have an important reference value for improving the sensitivity of the system detection. Liquid sampling atmospheric pressure glow discharge was found to be an ideal secondary excitation source. By studying the characteristic parameters of the plasma, we can further understand the excitation characteristics of the system [20]. The spectral characteristics of the solution cathode glow discharge are inseparable from the excitation process.

In the present work, the spectral and plasma characteristics of a hollow anode atmospheric pressure glow discharge (HA-APGD) were evaluated. The shape of the plasma, the emission intensity of the core elements, and the frequency of sound emission vary with the change in argon gas flow rate. Plasma parameters such as the electron excited temperature T_{exc} (H), rotational temperature T_{rot} (OH) and electron number density n_e of the excitation source plasma were characterized. The effects of these parameters on argon flow rate and its spatial distribution between the two electrodes were detected.

Experimental. *Experimental setup of HA-APGD (Fig. 1).* The peristaltic pump (BT100-2J, Longer, China) introduces the water sample into the capillary fused silica tube (0.7 mm inner diameter, 1.4 mm outer diameter). The glass tube is wrapped with a graphite rod (4 mm diameter) and the top of the glass tube is 3 mm higher than the graphite rod according to our previous work [21]. A hollow titanium tube (1 mm inner diameter, 2 mm outer diameter) is installed above the glass capillary. Argon gas is structured around the titanium tube into the plasma. A mass flow controller (D07-15, Seven-star, China) is applied to control the flow rate of argon, and the real time gas flow is displayed on a supervising instrument.

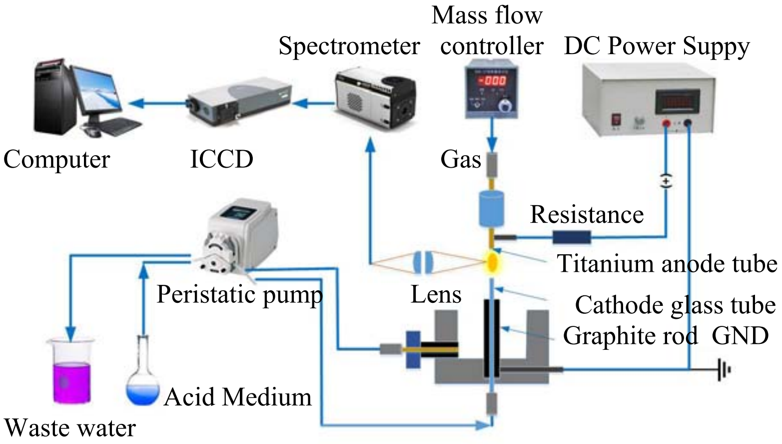

Fig. 1. The experimental setup of hollow anode solution cathode glow discharge (HA-APGD).

A DC high voltage power supply (P152/100MD1, Tianjin, China) provides a high voltage of more than 1000 V as an excitation source. The positive pole of the power supply is connected to the titanium tube with 2.27 kΩ ballast resistance to protect the power supply and stabilize the circuit. The graphite rod is equipped with the negative pole of the power supply. The radiation of plasma is collected by two plano-convex quartz lenses with a focal length of 60 mm, and then an optical fibre is connected with a spectrometer to collect optical signals. In the experiments, two spectrometers are used to obtain high- and low-resolution spectrum: a portable spectrometer (Ocean Optics, Maya 2000 Pro) and a three-grating spectrometer (Andor, Model SR-750). The former is used to capture a high band spectrum in order to calculate the electron excited temperature, and the latter is applied to measure other plasma parameters.

Reagents and samples. The sample was deionized water oxidized by nitric acid to pH 1, which was prepared from deionized water and concentrated HNO_3 solution (Chuandong chemical, 66%, China). The purification system (Ulupure, UIPR-II-10T, China) is used to prepare deionized water used in the experiment.

Results and discussion. *Spectroscopic identifications of HA-APGD.* Figure 2 shows the emission spectrum of molecular and atomic species in hollow anode-solution cathode glow discharge. Since the electrolyte cathode has severe electrolyte sputtering, the plasma composition changes rapidly after the plasma is ignited in the atmosphere. The introduction of anode gas may suppress sputtering, which makes the composition of the plasma relatively stable.

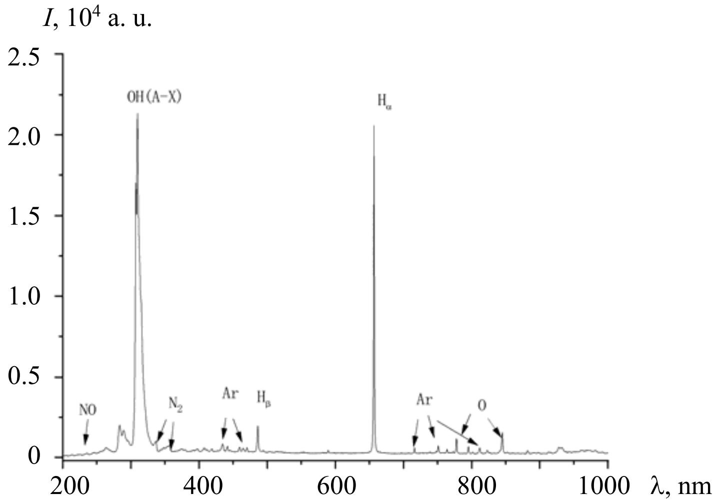

Fig. 2. The emission spectrum of molecular and atomic species in hollow anode-solution cathode glow discharge with a nitric acid solution at pH 1.

The OH ($A^2\Sigma^+ \rightarrow X^2\Pi$) emission at a spectral band head of 309.7 and 283.7 nm is generated from saturated water vapor ionization [22]. There is also a strong emission from atomic species including H_α (656.6 nm), H_β (486.1 nm) and O (777.2 and 844.9 nm) [33]. The emission line of Ar can be found in the range from 706.7 to 840 nm. NO (A-X) is collected at a spectral head of 226.3 nm. The N_2 second positive molecular system ($C^3\Pi_u \rightarrow B^3\Pi_g$) is seen as prominent bands across the range from 336.9 to 405.6 nm [23].

Effect of Ar flow rate on the spectral intensities of main species. Figure 3 shows the effects of argon flow rate on the spectral intensities of main species of the plasma. As shown in Fig. 3, with growth in argon gas flow, the emission intensity of H, Ar, O, and N_2 spectral lines near the cathode gradually increases. The emission intensity of NO increases more. In the region near the anode (0.7 mm away from the cathode), the low flow rate of argon is beneficial to enhance the production of these species (~78–177 mL/min), and then it gradually decreases at higher argon flow rates (~177–290 mL/min). However, the intensity change of NO species near the anode is not as obvious as in the cathode. We studied the relationship between species and Ar flow rate at the cathode and anode. This can be used as evidence for the existence of multiple excitation processes [23].

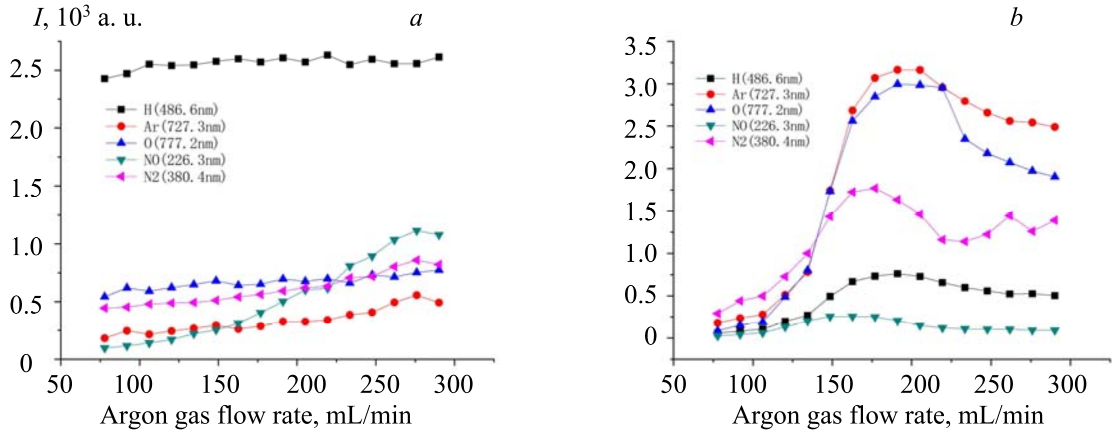

Fig. 3. The emission intensities of H, Ar, O, NO, and N_2 in the near cathode (a) and the near anode regions (b) versus the Ar flow rate.

The dissociation and recombination of H_2O^+ or H_3O^+ ions may be the main channel for the production of H (H_2) species in the discharge with a liquid cathode [24]. The blank sample contains dilute nitric acid. However, dilute nitric acid is relatively stable in nature and is not easily decomposed into NO. Thus, the reaction of the high-energy state of N (molecule or atom) with oxygen may be the cause of the NO excited state, e.g., $N+O_2=NO+O$, $N_2+O=NO+N$ [25]. An increase in argon flow may promote these reactions or cause the measured spectral intensity of NO to increase. The excited Ar state produces from the electron impacts the excitation, and the metastable Ar pooling reaction contributes to the excitation of the plasma [26]. However, when the flow rate of argon gas is too large, it may take too much energy. As a result, the spectral intensity is considered to be reduced.

In general, the spectral intensity of each specie or each of species at the cathode is generally lower than the intensity observed near the anode. In this system, the addition of argon can shield the air. The metastable-state generation of argon also promotes the energy transfer in the plasma.

Effect of Ar flow rate on the sound frequencies emitted by the plasma. During the maintenance of the discharge plasma, the sound is accompanied by the plasma's discharge process. The sound of the plasma is closely related to the flow rate of argon. Therefore, we collected the audio signals of HA-APGD and plotted the spectrogram. The audio signals emitted by the plasma at different argon gas flow rates were collected by a mobile phone, and then the audio signals were imported into a home-programmed Python program to draw the spectrogram. It turns out that the argon gas flow rate shows no obvious variation with the amplitude characteristics of the acoustic signal.

The effects of the plasma sound frequency on the flow rate of argon gas were also analyzed. Figures 4a,b present the time-frequency diagrams of audio signals when the Ar flow rate is 78 and 290 mL/min, respectively. As the red color deepens, the audio signal strength gradually increases. Figure 4c shows the frequency distribution of audio frequency at different argon flow rates. The audio signal of the plasma is mostly distributed in the low frequency area (about 2500 Hz) and barely appears at the high-frequency zone (about 10000 Hz).

As shown in Fig. 4c, the audio signal in the high frequency band is weakened with the argon flow rates improving. In addition, the range of sound distribution in the low frequency band becomes wider. In other words, the signal distribution changes from ~2000–3000 to ~2000–5000 Hz. When argon is transported at a low flow rate, the oscillation of the acoustic frequency is mainly due to the poor stability of the plasma. Therefore, we can infer that when the two ends of the electrode are in a high load state, the plasma obtains higher energy and causes a decrease in stability, which leads to a greater acoustic frequency oscillation. In addition, we know that the excitation mechanism of SCGD may be high temperature evaporation, or sputtering and spraying of cathode sample solution [27]. The direction of the argon gas flow rate is opposite to the cathode sputtering direction, which means that high gas flow rate will inhibit this sputtering and reduce the frequency of particle collisions. To better study the change in the plasma, images of the plasma at different target temperatures of argon flow rate were collected. Figures 4d,e displays the plasma at 92 and 276 mL/min argon flow rate. The plasma volume decreases as the argon flow rate increases, which may cause the mean free path of the particles to decrease. The narrowing of the passage between two poles may reduce the number of particles in the air that enters the plasma. So, the collision frequency of particles decreases. However, the cooling effect of the argon belt on the anode is very obvious. The anode in Fig. 4d is significantly redder, and the stray light generated by the overheating of the electrode will make a negative impact on the spectrum collection.

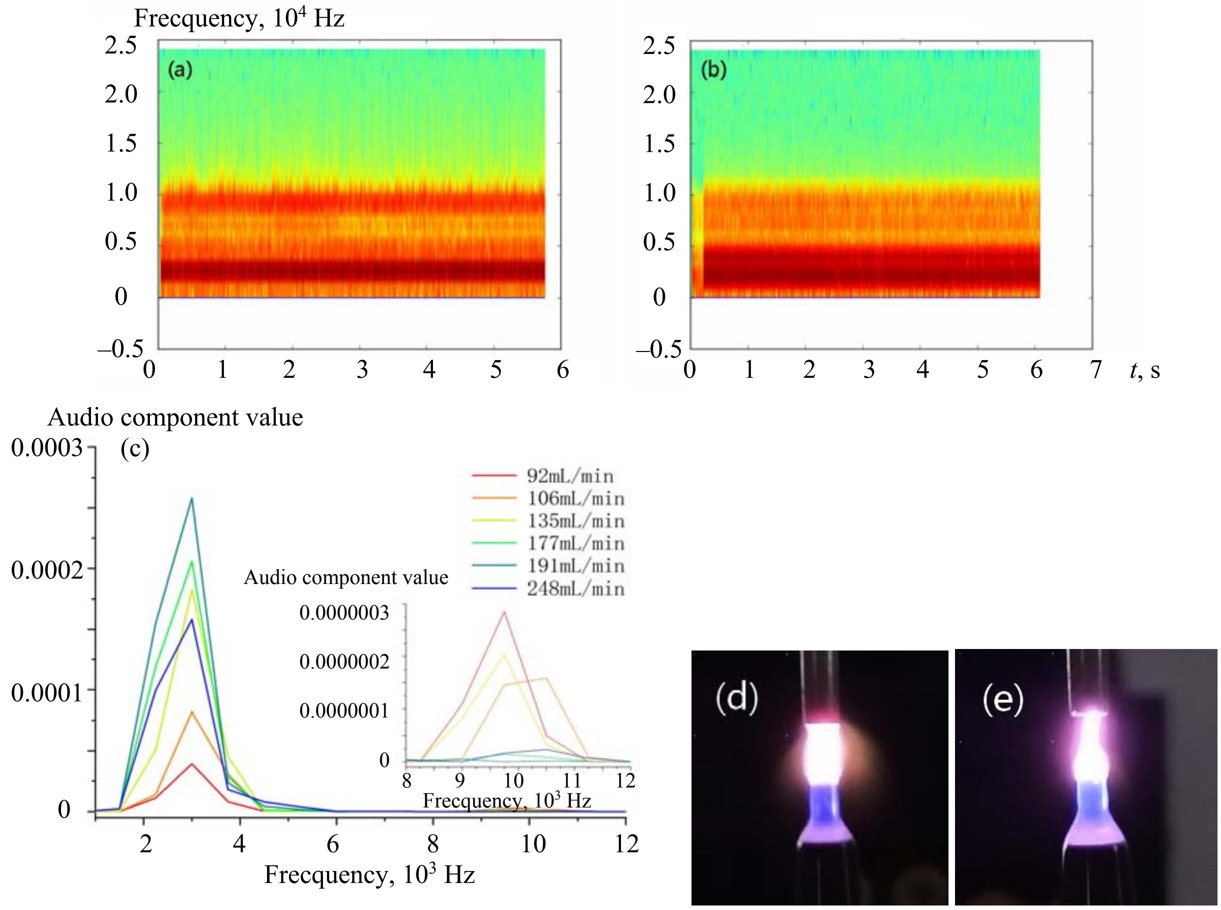

Fig. 4. Distribution diagram of sound frequency emitted by the plasma when Ar flow rate is 78 (a) and 290 mL/min (b) and sound frequency distribution curve with argon flow rate (c); plasma images at low argon flow rate (92 mL/min) (d) and high argon flow rate (276 mL/min) (e).

Determination of electron excited temperature. To further understand the ionization and excitation processes that occur in the plasma, we have studied the electron excited temperature (T_{exc}) [28]. Generally, there are two methods for calculating the electron excited temperature, which are the two-line method [29] and the Boltzmann diagonal method [30]. In this experiment, the two-line intensity ratio method is used to analyze the electron excited temperature of the APGD system. The plasma generated by the APGD system is a low-temperature plasma, which meets the local thermodynamic thermal equilibrium. The distribution of the atoms of the element at each energy level follows the Boltzmann distribution [31]. Therefore, according to the Boltzmann distribution principle of energy levels, the ratio of the spectral line intensities of two different energy level transitions can be expressed by the following formula:

$$\frac{I_1}{I_2}=\frac{A_1 g_1 \lambda_2}{A_2 g_2 \lambda_1}\exp\left(-\frac{E_2-E_1}{kT_e}\right), \tag{1}$$

where I_i, A_i, g_i, and k_i are the line intensity, transition probability, statistical weight, and transition wavelength of the energy level E_i, respectively; K is the Boltzmann constant.

As shown in Figs. 5a,b, the electron excited temperature is basically in the range of about ~3500–7000 K, which is similar to that of M. Kumai’s and Y. Takamura’s [32]. The value of the electron excited temperature is higher near the cathode and increases with growth in the argon flow rate. Compared with a typical APGD system with a metal anode, the increase in the electron excited temperature may be due to the presence of metastable Ar states. Introduction of argon gas can contribute to the transfer of energy [23]. As shown in Fig. 5a, with gradual growth in the argon flow rate, the excitation effect of the plasma tends to increase. The splash of liquid is reduced, so the intensity of electron excited temperature is higher compared with high argon flow rate.

In order to further understand the effect of the argon flow rate on the electron excited temperature, we calculated the Reynolds number (R_e). The Reynolds number (R_e) can be used to characterize fluid flow. It is defined as the ratio of the inertial forces (F_g) and viscous forces (F_m) of a fluid [33]:

$$R_e=\frac{F_g}{F_m}=\frac{\upsilon}{\eta}\rho D, \tag{2}$$

where υ is the flat and average velocity of the fluid, D is the diameter of the tube, η is the dynamic viscosity, and ρ is the fluid density.

Under standard conditions, the dynamic viscosity is 0.02083 MPa·s and the gas density is 1.7841 kg/m^3 for Ar [34]. The argon flow rate is in the range of 78 to 290 mL/min, and the Reynolds number obtained is within the range of 66.66 to 248.45. In this experiment, the gas flow was in a laminar state. This can explain why the range of change is narrow while the electron excited temperature increases with the flow rate of argon. The spatial distribution characteristics of the electron excited temperature were also further explored. The argon flow rate was 95 mL/min (this value was used in subsequent spatial distribution experiments). As can be seen in Fig. 5b, the electron excited temperature reaches its peak in the near cathode region. This may explain why most metal elements get a better excitation effect in the near cathode region [29].

Determination of rotational temperature. To understand the collision of plasma particles and the changes in energy transfer, the rotational temperature ($T_{\rm rot}$) was studied. P. Jamroz and W. Zyrnicki [35] proposed that the rotational temperature of the plasma can be calculated from the emission spectrum signal of the OH band ($A^2\Sigma^+\rightarrow X\,^2\Pi$). The rotational temperature can be calculated by the following formula [35]:

$$\ln\left(\frac{I\lambda}{A}\right)=b-\frac{E}{kT_{rot}}, \tag{3}$$

where A is the transition probability, E is the excitation energy, I is the signal strength, and K is the Boltzmann constant (8.617×10^{-5} eV/K).

As can be seen from Figs. 5c,d, the plasma’s rotational temperature is approximately in the range of ~850–1250 K. This result is roughly the same as that calculated by G. Faure and S. M. Shko’nik (~900–2500 K) [36]. The rotational temperature increases when the argon gas flow rate is 78~163mL/min and decreases slightly when the argon gas flow rate is ~163–290 mL/min. Figure 5d shows the spatial distribution of the rotational temperature. The rotational temperature near the metal anode is higher. The thermal conductivity of argon (0.017 W/m·K) is smaller than that of air (0.024 W/m·K), so more argon may reduce the loss of plasma energy. However, when the gas flow rate is high, its cooling effect will be increased, so this suppression effect may reach a certain balance with the previous promotion effect. The gas entering the excitation source from the anode will cause the anode to tend to the metastable state. Therefore, the energy exchange of particles in the anode region will be more frequent. Some scholars now use liquid anode systems to detect metal elements [37, 38].

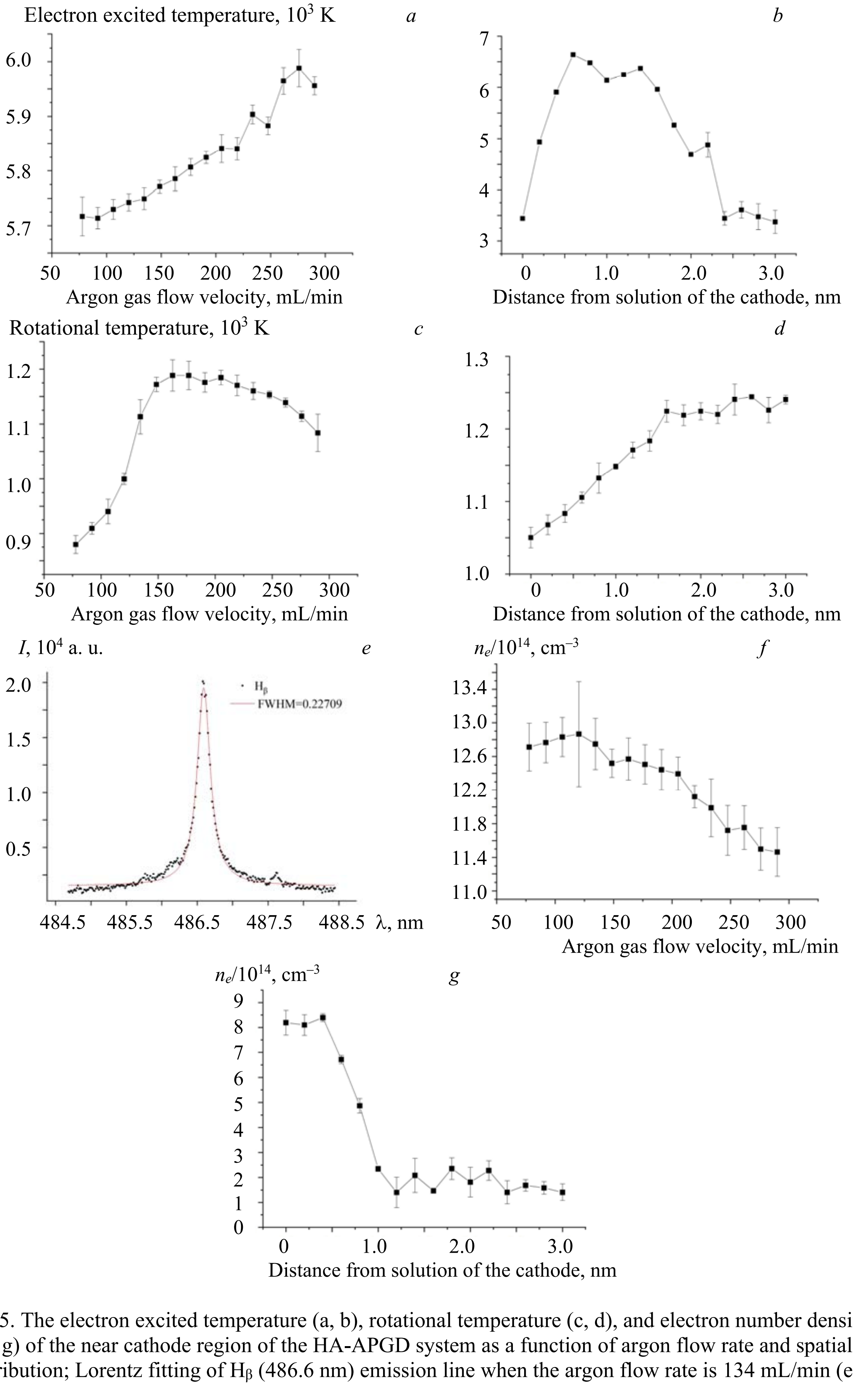

Fig. 5. The electron excited temperature (a, b), rotational temperature (c, d), and electron number density (f, g) of the near cathode region of the HA-APGD system as a function of argon flow rate and spatial distribution; Lorentz fitting of H_β (486.6 nm) emission line when the argon flow rate is 134 mL/min (e).

Determination of electron number density. There is a variety of diagnostic methods for diagnosing the electron number density (n_e) of plasma using optical emission spectrum [39, 40]. The H_β spectrum is often used to measure the electron density of the plasma in the Stark broadening method [41]. In this experiment, the emission spectrum of H_β line was first collected. The Lorentz fitting was then performed on the acquired spectral data by a computer. Figure 5e shows the Lorentzian fitting of H_β (486.6 nm) emission line when the argon flow rate is 134 mL/min. The Stark line width $\Delta\lambda_{1/2}$ was extracted from the measured line width $\Delta\lambda_{1/2(\mathrm{obs})}$ by subtracting the instrumental line broadening $\Delta\lambda_{1/2(\mathrm{instr})}$. In our case $\Delta\lambda_{1/2(\mathrm{instr})}$ was 0.06968 nm for H_β determined by measuring the FWHM of the Hg lines emitted by a standard low-pressure Hg lamp. The equation for calculating the electron number density is as follow [42]:

$$\left(\frac{\lambda_s}{4.800}\right)=\left(\frac{n_e}{10^{17}}\right)^{0.68116}. \qquad (4)$$

In Figure 5f the plasma electron number density decreases with the increase of argon flow rate. The results show that the electron number density of the HA-APGD system is in the range of (0.2–1.29)×10^{15} cm^{-3}. P. Mezei and T. Cserfalvi [43] commented on the published data on electron density in atmospheric glow discharges of electrolyte cathodes. The results showed that the value of electron density was between 10^{13} and 10^{14} cm^{-3}, which was lower than our results.

The decrease of n_e near the cathode region may be related to the enhancement of water sputtering and the subsequent increase in H_2O vapor and/or H_2O^+/H_3O^+ ion concentration during the discharge phase. The reduction in the energy and quantity of free electrons and other active materials is due to the presence of water vapor or its ionization during the discharge. This result is similar to the results obtained by Gielniak et al. [44] and Sismanoglu et al. [45]. Figure 5g illustrates the spatial distribution of electron number density between solution cathode and hollow anode. It is obvious that the electron number density near the cathode region reaches a very high level. The low electron number density of the anode could be due to the relatively stable nature of argon gas, which is difficult to ionize.

Generally, compared with excitation sources of other structures, the electron density of HA-APGD is much higher than those of the low-pressure glow discharge (~10^{11} cm^{-3}) [46] and the dc-APGD system (~10^{14} cm^{-3}) [30]. Therefore, the addition of argon gas is beneficial to increase the electron number density of the system.

Analytical plasma characteristics. Table 1 lists plasma parameters of this work and other published results. The electron number density is basically in the range of 10^{13}–10^{15} cm^{-3}. The electron number density value of HA-APGD is one order of magnitude higher than that of most systems, especially APGD without gas flow. Compared with the solid anode APGD system, the rotational temperature is significantly reduced by 1000 K. The increase of the plasma parameters is due to the improvement of the discharge mode and the introduction of various sheath gases or the two-stage structure. The rotational temperature decreases because the collision frequency of particles decreases by introducing/adding the gas.

TABLE 1. Comparison of Plasma Parameters of HA-APGD

Method	T_{exc}, K	T_{rot}, K	n_e, cm^{-3}	Reference
ELCAD	~6.000	~6.000	~2×10^{13}	[47, 48]
LS-APGD	~2.100–2.700	700–1.000	(2.6–3)×10^{15}	[20]
dc-μAPGD	11.000–1.5500	2.000–2.600	(0.2–1.1)×10^{15}	[48]
Pulsed-ELCAD	–	~2.100	~4.4×10^{14}	[49]
dc-APGD	5.700–19.000	2.400–3.050	(2.6–17.2)×10^{14}	[29]
Solid anode-dc-APGD	3.100–4200	2.700–4.100	-	[35]
This work	3.500–7.000	850–1.250	(0.2–1.29)×10^{15}	

Conclusions. An atmospheric pressure glow discharge was generated between solution cathode and hollow anode with miniature argon gas flow. The effects of argon flow rate on the spectral intensities of main species and plasma characteristics were studied. With increase in argon gas flow rate, the intensity of H, Ar, O, NO, and N_2 spectral lines increased slightly near the cathode and reached their maximum intensity at 177 mL/min near the anode. The audio signal in the high frequency band (about 10000 Hz) is weakened with the argon flow rates improving. Furthermore, the range of sound distribution in the low frequency band becomes wider (from 2000–3000 to 2000–5000 Hz). The volume of the plasma is reduced. The electron excited temperature of H T_{exc} (H), the rotational temperature of OH T_{rot} (OH), and the electron number density n_e of the HA-APGD system are 3500–7000, 12500–23000, 850–1250 K, and (0.2–1.29)×10^{15} cm^{-3}, respectively. The rotational temperature increases when the argon gas flow rate is 78~163 mL/min and decreases when the argon gas flow rate is 163–290 mL/min. As the flow rate of argon gas increases, the electron excited temperature increases and the electron number density decreases. The results show that the introduction of argon will affect the excitation process inside the plasma, and the stability of the plasma is closely related to the flow rate of argon. The metastable state will accelerate the energy conversion between particles. However, excessive gas flow rate may cool down the excitation source and reduce the gas temperature. The changes in plasma shape and frequency distribution also prove that the excess argon will reduce the collision frequency of particles. The above results will provide a basis for the study of electrolyte cathode glow discharge plasma.

Acknowledgments. This work was financially supported by the National Natural Science Foundation of China (61805030, 61705028), the Natural Science Foundation of Chongqing (cstc2020jcyj-msxmX0147), and the Science and Technology Research Program of Chongqing Municipal Education Commission (KJQN202000640).

REFERENCES

1. T. P. Liu, M. T. Liu, J. X. Liu, X. F. Mao, S. S. Zhang, Y. B. Shao, X. Na, G. Y. Chen, Y. Z. Qian, *Anal. Chem. Acta*, **1121**, 42–49 (2020).
2. M. K. Thakur, C. Y. Fang, Y. T. Yang, T. A. Effendi, P. K. Roy, R. S. Chen, K. O. Kostya, W. H. Chiang, S. Chattopadhyay, *ACS Appl. Mater. Interfaces*, **12**, 28550–28560 (2020).
3. H. Kabbara, S. Kasri, O. Brinza, G. Bauville, K. Gazeli, J. S. Sousa, V. Mille, A. Tallaire, G. Lombardi, C. Lazzaroni, *Appl. Phys. Lett.*, **116**, 171902 (2020).
4. M. K. Satapathy, Y. B. Manga, K. K. Ostrikov, W. H. Chiang, A. Pandey, R. Lekha, B. Nyambat, E. Y. Chuang, C. H. Chen, *ACS Appl. Mater. Interfaces*, **12**, 86–95 (2020).
5. T. A. Doroski, A. M. King, M. P. Fritz, M. R. Webb, *J. Anal. Atom. Spectrom.*, **28**, 1090–1095 (2013).
6. A. J. Schwartz, Z. Wang, S. J. Ray, G. M. Hieftje, *Anal. Chem.*, **85**, 129–137 (2013).
7. T. Cserfalvi, P. Mezei, P. Apai, *J. Phys. D. Appl. Phys.*, **26**, 2184–2188 (1993).
8. C. D. Quarles, A. J. Carado, C. J. Barinaga, D. W. Koppenaal, R. K. Marcus, *Anal. Bioanal. Chem.*, **402**, 261–268 (2012).
9. M. R. Webb, F. J. Andrade, G. M. Hieftje, *Anal. Chem.*, **79**, 7899–7905 (2007).
10. R. K. Marcus, C. Q. Burdette, B. T. Manard, L. X. Zhang, *Anal. Bioanal. Chem.*, **405**, 8171–8184 (2013).
11. K. Greda, P. Jamroz, P. Pohl, *J. Anal. Atom. Spectrom.*, **28**, 1233–1241 (2013).
12. P. H. Zheng, W. Q. Li, J. M. Wang, N. S. Wang, C. Zhong, Y. J. Luo, X. F. Wang, X. F. Mao, C. H. Lai, *Anal. Lett.*, **53**, 693–704 (2020).
13. J. M. Mo, Q. Li, X. H. Guo, G. X. Zhang, Z. Wang, *Anal. Chem.*, **89**, 10353–10360 (2017).
14. M. A. Dempster, R. K. Marcus, *Spectrochim. Acta B*, **55**, 599–610 (2000).
15. M. A. Dempster, W. C. Davis, R. K. Marcus, P. R. Cable-Dunlap, *J. Anal. Atom. Spectrom.*, **16**, 115–121 (2001).
16. K. Greda, P. Jamroz, P. Pohl, *J. Anal. Atom. Spectrom.*, **29**, 893–902 (2014).
17. K. Greda, K. Kurcbach, K. Ochromowicz, T. Lesniewicz, P. Jamroz, P. Pohl, *J. Anal. Atom. Spectrom.*, **30**, 1743–1751 (2015).
18. M. R. Webb, G. C. Y. Chan, F. J. Andrade, G. Gamez, G. M. Hieftje, *J. Anal. Atom. Spectrom.*, **21**, 525–530 (2006).
19. T. Verreycken, A. F. H. van Gessel, A. Pageau, P Bruggeman, *Plasma Sour. Sci. Technol.*, **20**, 024002 (2011).
20. B. T. Manard, J. J. Gonzalez, A. Sarkar, M. R. Dong, J. Chirinos, X. L. Mao, R. E. Russo, R. K. Marcus, *Spectrochim. Acta B*, **94**, 39–47 (2014).
21. J. M. Wang, P. F. Tang, P. C. Zheng, X. Zhai, *J. Anal. Atom. Spectrom.*, **32**, 1925–1931 (2017).
22. H. Liu, E. J. Lavernia, R. H. Rangel, *J. Phys. D. Appl. Phys.*, **26**, 1900–1908 (1993).
23. P. Jamroz, W. Zyrnicki, P. Pohl, *Spectrochim. Acta B*, **73**, 26–34 (2012).
24. P. Mezei, T. Cserfalvi, *Appl. Spectr. Rev.*, **42**, 573–604 (2007).
25. C. Lalo, J. Deson, C. Cerveau, R. I. Benaim, *Plasma Chem. Plasma P.*, **13**, 351–364 (1993).
26. Q. Li, X. Zhu, J. Li, Y. Pu, *J. Appl. Phys.*, **107**, 043304 (2010).

27. P. Mezei, T. Cserfalvi, M. Janossy, *J. Anal. Atom. Spectrom.*, **12**, 1203–1208 (1997).
28. W. H. Zhao, H. Z. Tang, Y. Shen, Y. Shi, L. Y. Hou, *Spectrosc. Spectr. Anal.*, **27**, 2145–2149 (2007).
29. J. M. Wang, M. He, P. C. Zheng, Y. Y. Chen, X. F. Mao, *Anal. Lett.*, **52**, 697–712 (2019).
30. Y. Liu, *J. Beijing Inst. Light Ind.*, **18**, 27–30 (2000).
31. X. B. Chen, X. S. Cai, X. L. Fan, J. Q. Shen, *Spectrosc. Spectr. Anal.*, **29**, 3177–3180 (2009).
32. M. Kumai, Y. Takamura, *Jpn. J. Appl. Phys.*, **50**, 096001 (2011).
33. S. V. Dresvin, J. Amouroux, *Adv. Heat Transf.*, **40**, 451–521 (2007).
34. P. C. Zheng, J. M. Wang, Z. F. Hu, H. G. Hao, Y. Wang, *High Volt. Apparatus*, **46**, 18–21 (2010).
35. P. Jamroz, W. Zyrnicki, *Plasma Chem. Plasma Process*, **31**, 681–696 (2011).
36. G. Faure, S. M. Shkol'nik, *J. Phys. D. Appl. Phys.*, **31**, 1212–1218 (1998).
37. K. Greda, M. Gorska, M. Welna, P. Jamroz, P. Pohl, *Talanta*, **199**, 107–115 (2019).
38. K. Swiderski, A. Dzimitrowicz, P. Jamroz, P. Pohl, *J. Anal. Atom. Spectrom.*, **33**, 437–451 (2018).
39. M. L. Shah, B. M. Suri, G. P. Gupta, *Eur. Phys. J. D.*, **69**, 16 (2015).
40. J. M. Gomba, C. D'Angelo, D. Bertuccelli, G. Bertuccelli, *Spectrochim. Acta B*, **56**, 695–705 (2001).
41. T. Cserfalvi, P. Mezei, *J. Anal. Atom. Spectrom.*, **18**, 596–602 (2003).
42. K. Greda, P. Jamroz, P. Pohl, *J. Anal. Atom. Spectrom.*, **28**, 134–141 (2013).
43. P. Mezei, T. Cserfalvi, *Sensors*, **12**, 6576–6586 (2012).
44. B. Gielniak, T. Fiedler, J. A. C. Broekaert, *Spectrochim. Acta B*, **66**, 21–27 (2011).
45. B. N. Sismanoglu, J. Amorim, J. A. Souza-Correa, C. Oliveira, M. P. Gomes, *Spectrochim. Acta B*, **64**, 1287–1293 (2009).
46. V. Kanicky, V. Otruba, J. Mermet, *Talanta*, **48**, 859–866 (1999).
47. P. Mezei, T. Cserfalvi, L. Csillag, *J. Phys. D. Appl. Phys.*, **38**, 2804–2811 (2005).
48. P. Mezei, T. Cserfalvi, *Eur. Phys. J. Appl. Phys.*, **40**, 89–94 (2007).
49. H. Yuan, D. Yang, X. Li, *Phys. Plasm.*, **26**, 053505 (2019).